JOURNAL OF GUIDANCE, CONTROL, AND DYNAMICS
Vol. 30, No. 4, July–August 2007

Long-Lifetime Lunar Repeat Ground Track Orbits

Ryan P. Russell*
Jet Propulsion Laboratory, California Institute of Technology, Pasadena, California 91109
and
Martin Lara†
Real Observatorio de la Armada, 11110 San Fernando, Spain

DOI: 10.2514/1.27104

A high degree and order lunar gravitational field is superimposed on the Earth–moon restricted three-body model to capture the dominating forces on a spacecraft in the vicinity of the moon. For the synchronously rotating moon, periodic orbits in this unaveraged model map repeat ground tracks and represent higher-order solutions to the frozen orbit problem. The stable or near-stable solutions are found over a wide range of defining characteristics, making them suitable for long-lifetime parking applications such as science orbits, crew exploration vehicle parking orbits, and global coverage constellation orbits. A full ephemeris is considered for selected orbits to evaluate the validity of the time-invariant, simplified model. Of the most promising results are the low-altitude families of near-circular, inclined orbits that maintain long-term stability despite the highly nonspherical lunar gravity. The method is systematic and enables rapid design and analysis of long-life orbits around any tidally locked celestial body with an arbitrarily high degree and order spherical harmonic gravity field.

Nomenclature

$a, e, i, \omega, \Omega, \upsilon$	=	classical orbital elements: semimajor axis, eccentricity, inclination, argument of periapse, longitude of ascending node, true anomaly
b_1, b_2	=	stability indices
C	=	Jacobi constant
$C_{n,m}, S_{n,m}$	=	nth degree and mth order nonzonal gravity field coefficients
d	=	normalized distance of the constraint vector
Gm_r	=	moon gravitational parameter
Gm_ρ	=	Earth gravitational parameter
h	=	ratio of the magnitude of the moon's nonspherical gravity acceleration to the tidal acceleration due to the Earth
J_n	=	nth degree zonal gravity field coefficient
$\boldsymbol{K}$	=	constraint vector
P_n	=	nth degree Legendre polynomial
$P_{n,m}$	=	nth degree and mth order associated Legendre function of the first kind
R	=	moon radius
r	=	distance to center of moon
T	=	period
t	=	time
U	=	spherical harmonic potential
$\mathbf{U}, \mathbf{V}, \mathbf{D}$	=	singular value decomposition matrices
$\boldsymbol{X}$	=	rotating, body-fixed state vector
X, Y, Z, U, V, W	=	nonrotating state components
x, y, z, u, v, w	=	rotating, body-fixed state components
Γ	=	potential function
δ	=	eigenvalue of full period state transition matrix
ε	=	near-zero tolerance parameter for identifying singular directions
λ, ϕ	=	longitude, latitude in body-fixed frame
μ	=	mass ratio
$\boldsymbol{\xi}$	=	unknown vector
ρ	=	distance to center of Earth
$\boldsymbol{\Phi}$	=	state transition matrix

Presented as Paper 6750 at the 2006 AIAA/AAS Astrodynamics Specialist Conference and Exhibit, Keystone, CO, 21–24 August 2006; received 7 August 2006; revision received 21 January 2007; accepted for publication 23 January 2007.

*Engineering Staff Member, Guidance, Navigation, and Control, 4800 Oak Grove Drive, M/S 301-121; Ryan.Russell@jpl.nasa.gov. Member AIAA.

†Commander, Ephemeris Section; mlara@roa.es. Member AIAA.

Introduction

WITH the recent interest in the return trips to the moon [1,2], trajectory designers are faced with a variety of challenges. The proposed missions will require extended stays and global communication coverage, much more so than during the Apollo era. It is well known that the highly nonspherical lunar gravity field leads to short-term impacts for the circular, polar, low-altitude orbiters of interest [3,4]. Furthermore, at the higher altitudes the Earth perturbations lead to eventual longer-term impacts [5,6]. Therein lays the challenge to find long-lifetime orbits in the vicinity of the Moon. Traditionally, mission designers seek orbits that are "frozen" [7–16] with regard to the eccentricity and argument of periapse as these highly coupled orbital elements generally have secular drifts due to the third-body and nonspherical gravity perturbations. Of course a secular drift in eccentricity leads directly to an impact orbit.

The frozen orbits are generally found by seeking equilibrium solutions to an averaged or reduced system [12]. In some cases, such as the near-circular two-body zonal problem [7,13,16], closed-form analytic series solutions are available. In general, the averaging procedure is essential, and the mathematics can be tedious and require "extensive algebraic manipulations" as p. 40 of [12] self describes. The complexity of the application and use of the resulting methods can be prohibitive for general use in preliminary space mission design. Furthermore, many of the higher-order effects are lost in the averaging or intentionally discarded through simplified models. When considering the third-body perturbations only, simple analytic solutions to the doubly averaged problem provide frozen orbits as well as a general characterization of motion [15].

References [7,10,13] represent significant progress in terms of simplifying the procedural effort required to find frozen orbits yet both remain limited to the two-body zonal problem, as is [12].

References [7,13] operate on the averaged system and are limited to orbits of low eccentricity, whereas Ref. [10] operates on the unaveraged system and is valid for all eccentricities. D'Avanzo et al. [16] provide further insight through the investigation of the Earth–sun effects on the frozen orbits of the near-circular, zonal problem, whereas [14] includes the averaged third-body potential directly in the calculation of frozen orbits including J_2, J_3, and $C_{2,2}$. Note that [10,16] are lunar–specific.

The still higher-order effects of the full unaveraged gravitational potential including the restricted third-body perturbations are yet to be investigated in the general frozen orbit problem. Here, we use the impressive speeds of modern computing to include both higher-order effects (unaveraged perturbations from restricted third-body effects and higher-order gravity potential), and the resulting dynamical system is therefore valid for a broad range of spacecraft altitudes. This higher-order force model and the ability to systematically find long-life orbits therein have immediate applications for rapid trajectory design across a wide spectrum of destinations. Examples include the moon, Earth, Mars, Venus, and high science priority planetary moon systems such as Jupiter–Europa and Saturn–Enceladus.

In this paper, techniques based on the recent design of long-life science orbits at Europa [17–19] are extended to specifically find long-life orbits at the moon. In particular, periodic orbits are sought in the restricted three-body model of the Earth–moon system plus a high-resolution lunar gravity field. The moon's rotational period is assumed to be synchronously locked with its orbital period (the rotation rate is equal to the orbital mean motion); thus, the periodic orbits are indeed repeat ground-track (RGT) orbits.

The concept of studying RGT orbits as true periodic orbits in an unaveraged model was first explored in detail in [20] and specifically applied to low-order gravity fields in the two-body Earth problem in [21] and later in the three-body Europa problem in [17]. Independently, the existence of periodic orbits in the zonal potential problem was also discussed in [22]. Repeat ground-track orbits are useful for many different missions, including mapping missions when the repeat cycle is long enough. Previous research shows that periodic orbits of simplified models generally remain as RGT orbits in full ephemeris models [17–19,21]. However, this does not apply to the "lumpy" moon where it has been shown that lower-order zonals notably affect the long-term behavior of low-altitude orbits [4,10]. The analysis in [8] supported by comments in [23] suggests that a 50 deg and order gravity field is necessary for accurate modeling of low-altitude lunar orbits. Therefore, in this paper a 50×50 lunar gravitational field is considered to capture the dominating higher-order effects. Although the conceptual methodology for periodic RGT orbit applications is developed in previous studies [17,20,21], we emphasize that the higher-fidelity gravity model extension and the numerical solution method outlined in the present study are new.

For simple resonances, or RGT cycles, the near-polar, near-circular solutions of the full potential plus restricted three-body problem are found to be linearly stable for altitudes less than $\sim$1200 km. At the higher altitudes, the families evolve into stable moderately inclined eccentric orbits. Solutions are documented for altitudes up to $\sim$2 moon radii. The families of solutions provide long-life orbits without requiring large-scale numerical searches [4]. The stable or near-stable families of solutions are shown to exist for a full range of average inclinations and altitudes, making them suitable for long-lifetime parking applications such as science orbits, crew exploration vehicle parking orbits, and global coverage constellation orbits [5,6].

A full ephemeris is considered for selected orbits to evaluate the validity of the time-invariant, simplified model. Because the invariant model accurately represents the lunar gravity but only approximates the Earth's gravity and ignores all other forces, the solutions from the invariant model map to the ephemeris model more favorably as the altitude is decreased. Accordingly, the lower-altitude ephemeris propagations enjoy the same long-life stability as predicted by the invariant model. Although the focus of the current application is on the moon, the methods and accompanying software are developed generally so as to immediately apply to other bodies of interest.

Dynamical Models

The Earth's third-body effect is modeled using the restricted three-body problem (RTBP) that assumes the Earth and moon orbit their common center of mass with a constant radius (in reality the radius varies $\pm 5.5\%$). The equations are normalized such that the separation is one length unit (LU) and the orbit period is 2π time units (TU). Given the additional assumption that the rotation of the moon is synchronous with its orbital period, the moon-fixed reference frame is identical to the moon-centered RTBP frame depicted in Fig. 1. In reality, a ± 8 deg libration results from the moon's elliptic orbit plus solar perturbations. Further, the lunar equatorial plane is inclined by 5.2 deg with respect to its orbital plane [23]. Therefore, the synchronous assumption is valid only to first order. Accordingly, the model will more closely approximate reality for low-altitude orbiters where the third-body effects are largely dominated by the nonspherical perturbations. Note that the International Astronomical Union (IAU) defined prime meridian and pole point in the direction of the Earth and the system angular momentum, respectively [24]. Both the tidal force field and the nonspherical force field are static in this rotating frame. It is emphasized that the accuracy of the higher-order gravity model is an artifact from orbit determination on past lunar missions. Although future missions will unquestionably improve the known accuracy, the gravity field is considered deterministic for purposes of this study.

The equations of motion for the restricted three-body plus full gravity model are given as

$$\mathrm{d}\boldsymbol{X}/\mathrm{d}t = \boldsymbol{f}(\boldsymbol{X}) \tag{1}$$

$$\boldsymbol{X} = \begin{bmatrix} x \\ y \\ z \\ u \\ v \\ w \end{bmatrix} \qquad \boldsymbol{f} = \begin{bmatrix} u \\ v \\ w \\ 2v + \partial\Gamma/\partial x \\ -2u + \partial\Gamma/\partial y \\ \partial\Gamma/\partial z \end{bmatrix} \tag{2}$$

where a potential function Γ is introduced,

$$\begin{aligned} \Gamma &= (x - 1 + \mu)^2/2 + y^2/2 + (1 - \mu)/\rho + (\mu/r + U) \\ \mu &= Gm_r/(Gm_\rho + Gm_r) \qquad \rho = \sqrt{(x-1)^2 + y^2 + z^2} \\ r &= \sqrt{x^2 + y^2 + z^2} \end{aligned} \tag{3}$$

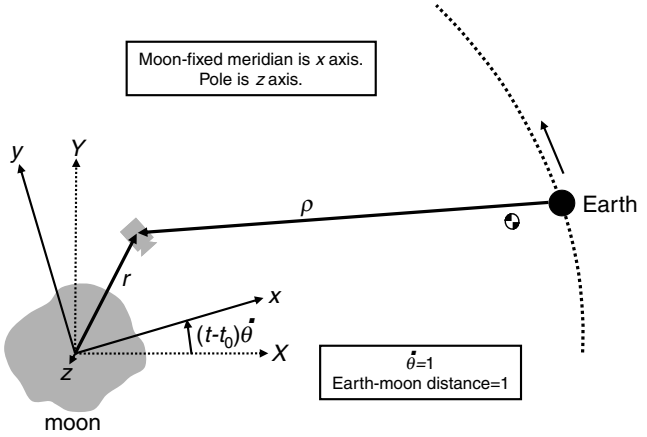

Fig. 1 Moon-centered restricted three-body model plus full lunar gravity field. For the synchronously rotating moon, the (*xyz*) reference frame is coincident with the body-fixed moon frame.

Table 1 Earth and moon parameters

Parameter	Symbol	Value
Moon gravitational parameter	Gm_r	4,902.801076 km^3/s^2
Earth gravitational parameter	Gm_p	398,600.4415 km^3/s^2
Mass ratio (derived)	μ	0.01215058655960256
Moon mean radius[a]	R	1,738.0 km
Earth–moon distance (length unit)	LU	384,400 km
Time unit (derived)	TU	375,190.258663027 s

[a]Spherical harmonic expansion radius from lp150q model.

U is the contribution due to the nonspherical moon and is expressed via the standard spherical harmonic expansion. For completeness, we provide in the Appendix several useful equations summarized from [25].

The system is Hamiltonian and admits an integral of motion C, given in Eq. (4):

$$C = 2\Gamma - (u^2 + v^2 + w^2) \tag{4}$$

For conversion to classical orbital elements, the rotating frame is defined to be aligned with the nonrotating frame at $t = t_0$ (see Fig. 1) and the transformation into the nonrotating frame is given in Eq. (5):

$$\begin{aligned} \begin{bmatrix} X & Y & Z \end{bmatrix}^\top &= \mathbf{R}\begin{bmatrix} x & y & z \end{bmatrix}^\top \\ \begin{bmatrix} U & V & W \end{bmatrix}^\top &= \mathbf{R}\{\begin{bmatrix} u & v & w \end{bmatrix}^\top + \begin{bmatrix} 0 & 0 & 1 \end{bmatrix}^\top \\ &\quad \times \begin{bmatrix} x & y & z \end{bmatrix}^\top\} \\ \mathbf{R} &= \begin{bmatrix} \cos(t-t_0) & -\sin(t-t_0) & 0 \\ \sin(t-t_0) & \cos(t-t_0) & 0 \\ 0 & 0 & 1 \end{bmatrix} \end{aligned} \tag{5}$$

The spherical harmonic representation of the lunar gravity field is taken from the publicly available[‡] lp150q model, a 150×150 deg solution produced by the Lunar Prospector Gravity Science Team led by A. S. Konopliv at the Jet Propulsion Laboratory. The estimation includes all available data from past American missions to the moon. Permanent tide adjustments of $\Delta J_2 = 9.32206780233229\text{E-}08$ and $\Delta C_{2,2} = 4.66066496097581\text{E-}08$ are required [23]. A 3×3 subset of the normalized lp150q gravity field including the adjustments is given in Eq. (6). For purposes of this study, it is emphasized that the lunar gravity field includes the 50×50 truncated version of the lp150q model. Table 1 provides the mass and distance parameters specific to the Earth–moon system.

$$\begin{aligned} &\bar{J}_2 = 0.909427845027\text{E-}04 && \bar{J}_3 = 0.320307167959\text{E-}05 \\ &\bar{C}_{2,1} = -0.186273608184\text{E-}08 && \bar{C}_{2,2} = 0.347098301319\text{E-}04 \\ &\bar{C}_{3,1} = 0.263418358622\text{E-}04 && \bar{C}_{3,2} = 0.141853316786\text{E-}04 \\ &\bar{C}_{3,3} = 0.122862645044\text{E-}04 && \bar{S}_{2,1} = -0.142453894610\text{E-}08 \\ &\bar{S}_{2,2} = 0.144063503540\text{E-}07 && \bar{S}_{3,1} = 0.546307860882\text{E-}05 \\ &\bar{S}_{3,2} = 0.488913911795\text{E-}05 && \bar{S}_{3,3} = -0.178246270720\text{E-}05 \end{aligned} \tag{6}$$

For selected ephemeris propagations, the states of the planets and the moon are based on publicly available[§] data from the Jet Propulsion Laboratory. The poles and prime meridians for the Earth and moon are based on the most recent data from the IAU Working Group on Cartographic Coordinates and Rotational Elements of the Planets and Satellites [24]. The lunar gravity field is the same as used in the restricted three-body plus 50×50 gravity model whereas the only nonspherical term considered for the Earth is $J_2 = 0.0010826$. The active bodies for the ephemeris model include the sun, the moon, and all the planets.

[‡]Data available online at http://pds-geosciences.wustl.edu/geodata/lp-l-rss-5-gravity-v1/lp_1001/sha/jgl150q1.lbl [cited 12 March 2006].

[§]Data available online at http://naif.jpl.nasa.gov/naif/spiceconcept.html [cited 12 March 2006], ftp://naif.jpl.nasa.gov/pub/naif/generic_kernels/spk/planets/de403.bsp [cited 12 March 2006], ftp://naif.jpl.nasa.gov/pub/naif/generic_kernels/pck/pck00008.tpc [cited 12 March 2006].

Periodic Orbit Generation

The symmetries typically associated with the RTBP and the zonal problem are no longer valid when considering an arbitrary lunar gravity field. Thus, a full-dimensioned differential corrector is sought to find periodic orbits in the general nonsymmetric case. The Jacobi integral C is a natural parameter to vary for generating families of solutions. Therefore, the constraint vector $\boldsymbol{K}$ consists of the periodicity conditions and the Jacobi integral target and is given in Eq. (7). The unknown vector $\boldsymbol{\xi}_0$ consists of each initial state variable except z_0, where the period and z dimensions are removed by setting $z_0 = 0$ and implicitly stopping the integration exactly at $z_T = 0$ (to machine precision), where T is the period (this discrete mapping technique is a proven strategy to reduce dimensions and is described in more detail in [26–29]):

$$\boldsymbol{K} = \begin{pmatrix} \boldsymbol{\xi}_T & -\boldsymbol{\xi}_0 \\ C & -C_* \end{pmatrix}_{6\times 1}, \qquad \boldsymbol{\xi} = \begin{pmatrix} x & y & u & v & w \end{pmatrix}^\top \tag{7}$$

Assume that an initial guess $\boldsymbol{\xi}_0$ in the vicinity of a solution yields a nonzero $\boldsymbol{K}$. To drive the constraint vector to zero, a $\Delta\boldsymbol{\xi}_0$ is sought that satisfies the linear system,

$$\frac{\mathrm{d}\boldsymbol{K}}{\mathrm{d}\boldsymbol{\xi}_0}\Delta\boldsymbol{\xi}_0 = -\boldsymbol{K} \tag{8}$$

Note that there are five unknowns and six constraints as stated in Eq. (8). To ensure a unique solution (given a nonsingular Jacobian) some researchers reformulate the problem to have an equal number of constraints and unknowns [30,31]. On the contrary, in this study a least-squares solution method allows for all of the constraints to be enforced regardless of the number of unknowns. A subtle point deserves mentioning here. A least-squares approach generally provides the best-fit solution to an overconstrained problem. However, as will be discussed shortly, there are frequently multiple directions in the phase space where periodic solutions exist, making the fundamental problem underconstrained if the singular directions are not removed from the search space. Therefore, despite that the problem as stated in Eq. (8) is overconstrained, the dynamics suggest that solutions exist that satisfy all of the constraints. Thus, if such solutions exist, then the least-squares correction will drive the norm of the constraint vector to zero.

Singular value decomposition provides a simple solution to the problem of the degenerate Jacobian associated with a periodic orbit. The dimension of the null space of such a Jacobian is nonzero because any direction tangent to the solution leads again to a periodic solution. This degeneracy is compounded in the special case of a bifurcation periodic orbit, where there is an additional degenerate direction that leads to a new periodic orbit. The dimension-reducing techniques discussed in [29–32] deal effectively with the tangent degeneracy, but fail to address the special case of the bifurcation orbit. Unfortunately, all of the high-resonant lunar orbits that are the subject of this study are bifurcation orbits. To address both the bifurcation orbit and the tangent degeneracy, the singular value decomposition of the nonsquare Jacobian in Eq. (8) provides an elegant mechanism to reduce the system only in the degenerate directions, as opposed to the arbitrary directions proposed in [30,31]. The 6×5 Jacobian has a singular value decomposition of the form

$$\frac{\mathrm{d}\boldsymbol{K}}{\mathrm{d}\boldsymbol{\xi}_0} = \mathbf{U}\mathbf{D}\mathbf{V}^\top \tag{9}$$

where $\mathbf{U}$ and $\mathbf{V}$ are square orthogonal matrices of dimension 6 and 5, respectively, and $\mathbf{D}$ is a 6×5 matrix with nonnegative entries on the diagonal and zeroes otherwise. See [33] for details on singular value decomposition. The pseudoinverse of the Jacobian as indicated by the superscript $+$ is given in Eq. (10) and leads to the least-squares solution to the overconstrained system in Eq. (8) (see [34] for a

further description of a least-squares application to differential orbit correction):

$$\left(\frac{\mathrm{d}\boldsymbol{K}}{\mathrm{d}\boldsymbol{\xi}_0}\right)^+ = \mathbf{VSU}^\top, \qquad S_{i,i} = \begin{cases} 1/D_{i,i} & \text{for } D_{i,i} > \varepsilon \\ 0 & \text{for } D_{i,i} < \varepsilon \end{cases} \tag{10}$$

The diagonal elements of $\mathbf{D}$ are called the singular values of the Jacobian. A singular matrix has at least one singular value of zero, whereas an ill-conditioned matrix has at least one near-zero singular value. For practical computations, any singular value less than ε is considered zero as indicated in Eq. (10). Equation (11) gives the least-squares solution to Eq. (8). Furthermore, as Lay [33] explains, when one or more the singular values are zero (or $<\varepsilon$), then the solution given by Eq. (11) is the least-squares solution with the smallest magnitude:

$$\Delta\boldsymbol{\xi}_0 = -(\mathbf{VSU}^\top)\boldsymbol{K} \tag{11}$$

Therefore, the problem associated with any degenerate directions is solved through the simple selection of ε and the application of Eq. (10). Furthermore, all of the constraints are active because there is no requirement for the Jacobian to be square. The Jacobian is calculated from

$$\frac{\mathrm{d}\boldsymbol{K}}{\mathrm{d}\boldsymbol{\xi}_0} = \begin{pmatrix} \frac{\mathrm{d}\boldsymbol{\xi}_T}{\mathrm{d}\boldsymbol{\xi}_0} - \mathbf{I}_{5\times5} \\ \frac{\mathrm{d}C}{\mathrm{d}\boldsymbol{\xi}_0} \end{pmatrix}_{6\times5} \tag{12}$$

$$\frac{\mathrm{d}\boldsymbol{\xi}_T}{\mathrm{d}\boldsymbol{\xi}_0} = \frac{\partial\boldsymbol{\xi}_T}{\partial\boldsymbol{\xi}_0} + \frac{\partial\boldsymbol{\xi}_T}{\partial T}\frac{\partial T}{\partial\boldsymbol{\xi}_0} \tag{13}$$

where the partial derivative of period with respect to the initial conditions is found from

$$\Delta z_T = \frac{\partial z_T}{\partial\boldsymbol{\xi}_0}\delta\boldsymbol{\xi}_0 + \dot{z}_T\delta T \tag{14}$$

Because the integrator implicitly stops on the xy plane, Eq. (14) can be solved with $\Delta z_T = 0$, giving

$$\frac{\partial T}{\partial\boldsymbol{\xi}_0} = -\frac{\partial z_T}{\partial\boldsymbol{\xi}_0}\frac{1}{\dot{z}_T} \tag{15}$$

Finally, Eq. (13) is rewritten as

$$\frac{\mathrm{d}\boldsymbol{\xi}_T}{\mathrm{d}\boldsymbol{\xi}_0} = \boldsymbol{\Phi}(T,t_0)_{i\neq3,j\neq3} - \frac{1}{\dot{z}_T}\dot{\boldsymbol{\xi}}_T\boldsymbol{\Phi}(T,t_0)_{i=3,j\neq3} \tag{16}$$

where $\boldsymbol{\Phi}$ is the state transition matrix that provides the partial derivatives of the state from one time to another across a continuous trajectory. Thus,

$$\boldsymbol{\Phi}(t,t_0) = \partial\mathbf{X}(t)/\partial\mathbf{X}(t_0) \tag{17}$$

The state transition matrix is obtained by integrating the variational equations given in Eq. (18) along with Eq. (1). The calculation of the partial derivative in Eq. (18) is straightforward but tedious due to the inclusion of the full gravity potential in $\boldsymbol{f}$ as described in Eqs. (2), (3), and (A1–A7) (for brevity, the equations are left out here):

$$\dot{\boldsymbol{\Phi}}(t,t_0) = (\partial\mathbf{f}/\partial\mathbf{X})|_t\boldsymbol{\Phi}(t,t_0) \qquad \boldsymbol{\Phi}(t_0,t_0) = \mathbf{I}_{6\times6} \tag{18}$$

To summarize, given that an initial guess $\boldsymbol{\xi}_0$ is in the vicinity of a solution and yields a constraint violation $\boldsymbol{K}$, the linearized first-order correction is given by Eq. (11). Depending on the validity of the initial guess, it is often useful to scale the correction step to prevent any of the step directions from exceeding any of the user-defined maximum step sizes. The process is iterated with the corrected guess until convergence as indicated by a constraint violation that is sufficiently small and is no longer reducing in length. The scalar normalized miss distance d is defined in Eq. (19), where $\|\ \|$ is the Euclidean two-norm operator:

$$d = \|\boldsymbol{X}(t_f)_{i=1,2,3} - \boldsymbol{X}(t_0)_{i=1,2,3}\|/\|\boldsymbol{X}(t_0)_{i=1,2,3}\| + \|\boldsymbol{X}(t_f)_{i=4,5,6} - \boldsymbol{X}(t_0)_{i=4,5,6}\|/\|\boldsymbol{X}(t_0)_{i=4,5,6}\| + \|(C-C^*)/C^*\| \tag{19}$$

Note that the selection of ε affects the convergence properties of the differential correction process and is related to the achievable minimum d. If ε is too large, the algorithm will overconstrain the search space and the d value will stabilize at a larger value. If ε is too small, the algorithm will underconstrain the search space (identify too few singular directions), and d will oscillate indefinitely as the algorithm repeats the pattern of approaching the solution then falling off due to the singularity. For this study, ε values in the range of $10^{-6} \rightarrow 10^{-4}$ are found to be sufficient such that d will approach and stabilize to small values ($\sim10^{-11}$).

The stability of the converged solution is evaluated based on the full period state transition matrix, also known as the Monodromy matrix. It is well known that the eigenvalues of the Monodromy matrix for conservative autonomous systems occur in reciprocal pairs [35]. Furthermore, tangent variations maintain periodicity. Therefore, the eigenvalues of the Monodromy matrix will have the form $\{\delta_1, 1/\delta_1, \delta_2, 1/\delta_2, 1, 1\}$. The complex stability indices are defined in Eq. (20), where $|b_i| \leq 2$ and b_i must be real for linear stability (for detailed discussions on the state transition matrix, the Monodromy matrix, and stability, see [30,35–37]):

$$b_1 = \delta_1 + 1/\delta_1 \qquad b_2 = \delta_2 + 1/\delta_2 \tag{20}$$

Families of Solutions

Periodic orbits in the perturbed RTBP enjoy the integral of motion C, given in Eq. (4). The natural family of a single solution is found by successively seeking neighboring solutions for small fixed variations in C.

For orbits close to the primary, energy variations generally lead to one of the two following effects: inclination variations with near-fixed eccentricity or eccentricity variations with near-fixed inclination that is commonly referred to as the "critical inclination" [12,38]. The series solution expressions for the classic frozen orbits find singularities at this critical inclination. Although the search for periodic orbits finds related degenerate bifurcations near this same inclination, it will be shown (for the lunar families considered) that the singular value decomposition approach described in this paper effectively follows families through both sides of the bifurcations.

For the high-altitude near-polar solutions, varying C across a family of orbits has the same effect as varying the average i. From a mission designer's perspective, i is an extremely important parameter when considering specific mission objectives and constraints.

For the near-circular inclined class of orbits sought in this study, the main characteristic that distinguishes one family from another is the integer ratio of spacecraft revolutions to body revolutions during a full period. In this paper, the number of spacecraft revolutions is varied while number of body revolutions is fixed to one. Accordingly, all solutions of an n-cycle family complete one period after exactly n spacecraft revolutions. The normalized period of each periodic solution is exactly one period of the body's revolution (2π) plus the total change in the longitude of the ascending node of the spacecraft orbit. The altitude, a second parameter of great importance to mission design, is controlled through the selection of n, where higher values of n correspond to lower altitudes.

To seek families of solutions that vary in C, the following algorithm is employed:

1) Select n, indicating the n-cycle family is sought.

2) Provide initial guess: Assuming a two-body orbit around a point mass moon, calculate the initial conditions starting in the plane of the moon's equator for a polar orbit that completes n revolutions during one lunar revolution.

3) Use the initial guess and Eqs. (7–18) to converge on a periodic solution of the n-cycle family. Because this is the first member of the family, the Jacobi constant of the near-polar solution is unknown.

Accordingly, the C constraint is removed from $\boldsymbol{K}$ in Eq. (7) and the dimensions of the following equations are appropriately modified. Thus, the inclination of the initial guess is polar, yet the solution is free to converge to any inclination. Generally, because the solution method is local, the algorithm converges to a near-polar periodic solution. Note, the near-polar solution is sought initially because the two-body solution is a better guess at the near-polar inclinations and generally converges in the full perturbed RTBP model. For complex gravity fields like the moon's, it may be necessary to parametrically solve several subproblems in which the first subproblem includes the third-body effects, and each successive problem includes an increasingly complex gravity field and uses the initial conditions from the previous subproblem.

4) Follow the initial near-polar solution in both directions for small variations in $\pm C$ until the user-supplied minimum or maximum is reached. A predictor–corrector scheme based on Eq. (11) is used for the continuation of a solution along its natural family. For the predictor step, the initial guess for each successive solution is found by solving Eq. (11), where the partial derivatives and C are evaluated along the previous periodic solution and $\boldsymbol{K}$ is $[0, 0, 0, 0, 0, C - C^*]^\top$, where C^* is the new desired value for the Jacobi constant. The predicted initial condition is propagated for n cycles and is corrected using Eq. (11) and the full $\boldsymbol{K}$ from Eq. (7). The corrector step is iterated until convergence.

Families that vary in altitude yet maintain similar inclination are not continuous families because the generating parameter n is integer valued. Nonetheless, these insightful groupings are found by repeating the first three steps of the algorithm for a desired range of n.

Example RGT Families and Orbits

For large variations in altitude, near-polar RGT solutions are sought for n values of 73 to 328 cycles at increments of 15. Note that 328 cycles is chosen as an upper bound because it gives a typical low-altitude 2 h lunar orbit, whereas 73 cycles is the arbitrarily chosen lower bound because it gives an orbit altitude of approximately two lunar radii. Figure 2 shows the results in which each solution is initiated with a 90.5 deg two-body circular orbit. Because the Jacobi integral is left unconstrained, the solutions are free to evolve to any inclination (although a max-step size of 10 km in position and .1 km/s in velocity constrains the solution to stay in the vicinity of the guess). For these near-polar solutions, as the minimum altitude decreases from 3319 to 39 km, the average eccentricity increases from $\sim$0 to $\sim$0.04. Note, the miss distance d is consistently near 10^{-12} normalized units, indicating the initial and final conditions are equivalent to approximately 12 significant digits. Of the most important observations from Fig. 2 is the unstable to stable transition that occurs near 168 cycles at an approximate altitude of $\sim$1200 km as indicated by the boundary where both stability indices equal 2. Also, note that the average ratio of the magnitudes of the harmonic to the tidal perturbing forces is unity at an approximate altitude of $\sim$2000 km.

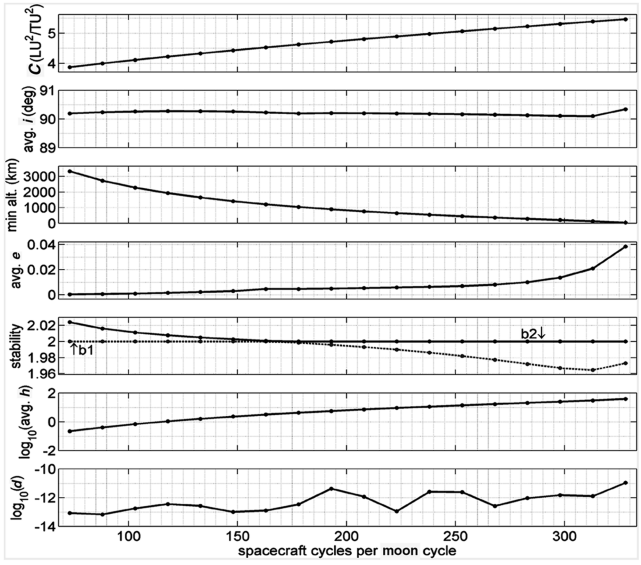

Fig. 2 Characteristics of near-polar RGT solutions for n cycles of 73 to 328. d is the periodicity precision defined in Eq. (19).

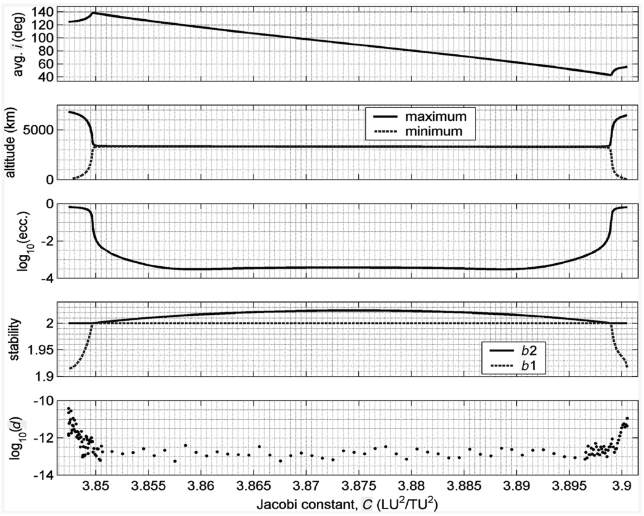

Fig. 3 Characteristics of the 73-cycle RGT family.

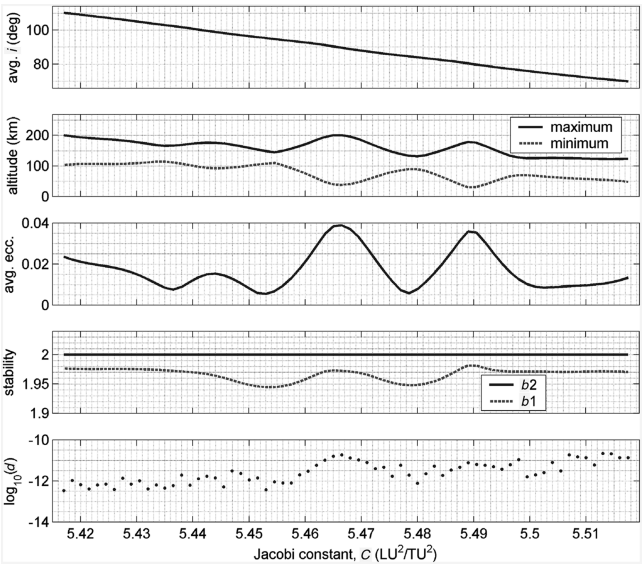

Fig. 4 Characteristics of the 328-cycle RGT family.

For a given n-cycle orbit from Fig. 2, its natural family is found for small variations in C. As examples, the high-altitude, 73-cycle and the low-altitude, 328-cycle natural families are presented in Figs. 3 and 4. Figure 3 shows that the high-attitude family consists of mildly unstable orbits with very low eccentricities for a wide range of inclination centered at 90 deg while the family ends in both C directions with stable highly eccentric impact orbits. All of the near-circular orbits are mildly unstable where the maximum instability is represented by the shallow maximum in b_2 that occurs near $i = 90$ deg. The eccentricities grow rapidly in both directions as the family passes through the bifurcation inclinations of approximately 43 and 139 deg where both stability indices equal 2. Outside of the critical points, a reflection in inclination occurs until the family ends with stable impact orbits of $\{C, i, e\} \sim \{3.8474\,\mathrm{LU}^2/\mathrm{TU}^2, 125\ \mathrm{deg}, 0.656\}$ and $\{3.9005\,\mathrm{LU}^2/\mathrm{TU}^2, 55.6\ \mathrm{deg}, 0.644\}$.

Despite the higher-fidelity force model, the existence and location of the stable eccentric orbits are consistent with the frozen orbits around the Earth and moon discussed in [6,7,10–12,20,21]. The higher-order effects of the unaveraged equations and the full nonspherical gravity are appreciated in the difference between the

RGT bifurcation inclination of ∼43 deg compared to the critical inclination in the doubly averaged third-body problem of ∼40 deg. Although Fig. 2 indicates that the tidal perturbations are greater than the nonspherical gravity perturbations for the near-circular 73-cycle solutions, the close lunar approaches of the eccentric solutions raise the significance of the nonspherical gravity. Note that the RGT bifurcation inclinations change slightly for orbits with different altitudes and lunar gravity models.

It is worth noting that different 73-cycle families of RGT orbits are found by starting near the direct or retrograde planar orbits. These families begin as stable near-circular orbits and reflect in C near the bifurcation inclination where they transition to stable eccentric orbits with closest approach over the southern lunar pole ($\omega \sim -90$ deg). These orbits have the opposite orientation from the eccentric orbits of the family shown in Fig. 3, in which the closest approach is over the northern pole ($\omega \sim +90$ deg). Although the search method is applicable for periodic families of multiple types, the attention of this study is focused on the families centered on the polar inclinations because of their favorable global coverage.

Figure 4 shows the evolution of the low-altitude 328-cycle natural family. The evolution of the eccentricity vs inclination curve finds general agreement with the lower-order frozen lunar orbits found in [7–11,39], noting that the best agreement is with those reported in [9] based on the LGM0281 gravity field. The stability indices from Fig. 4 show linear stability for the full range of near-polar inclinations. The highly nonspherical gravity field manifests through large variability in the average eccentricities. There are two noteworthy minimums occurring near inclinations of 85 and 95 deg, whereas the most polar orbit finds a maximum eccentricity of ∼0.04. The near-zero eccentricity solutions are consistent with the frozen lunar orbits found in the literature. However, the inclusion of the third-body and the nonzonal terms destroys the existence of the exactly circular frozen orbits. The smallest variation in altitude occurs at an average inclination of 94.8 deg with minimum and maximum altitudes of 110 and 144 km. The higher-order effects of including the nonzonal terms as well as the third-body perturbations are further appreciated in the loss of symmetry with respect to $i = 90$ deg. Although symmetry remains to first order as the two-body zonal problem predicts [7,12], the peak in eccentricity that occurs near $i = 80$ deg is more than twice as high as the peak that occurs at $i = 100$ deg. This lack of symmetry is also evident in the altitude and stability plots.

Figures 5–7 illustrate three example point solutions from the 73- and 328-cycle families. These solutions are termed orbits A, B, and C, respectively. The initial conditions and other characteristics for the example solutions are given in Table 2. Note that the degeneracy associated with one of the stability indices always being 2 indicates that the solutions are not necessarily unique. Thus, qualitatively similar solutions with minor differences in initial conditions are possible to achieve, despite having the same C value. This is consistent with the findings in [21]. Although all RGT orbits are periodic in each of the six rotating Cartesian coordinates by definition, Figs. 5–7 show that each of the orbital elements is periodic except the longitude of ascending node, Ω. (It was noted previously that $\Delta\Omega = T - 2\pi$.) The short period oscillations seen in the orbital elements of orbits A–C result from each spacecraft revolution, whereas the long-period oscillations result from the variability of the perturbing force field as the orbit plane rotates around the body. The large erratic variations in the long-period motion of orbit C, the low-altitude 328-cycle orbit, are indicative of the notoriously lumpy lunar gravitational field. As further evidence, the argument of periapse, while centered on the $\omega \sim -90$ deg as the zonal problem predicts, appreciates nontrivial variations of ± 17 deg during the course of one period. These large variations in argument of periapse are common to all members of the 328-cycle family. Note that the mean is near $\omega \sim -90$ deg for all of the orbits considered in Fig. 4 except those in the inclination ranges of $75 < i < 84$ deg and $95 < i < 103$ deg, where the mean is shifted to $\omega \sim +90$ deg. The

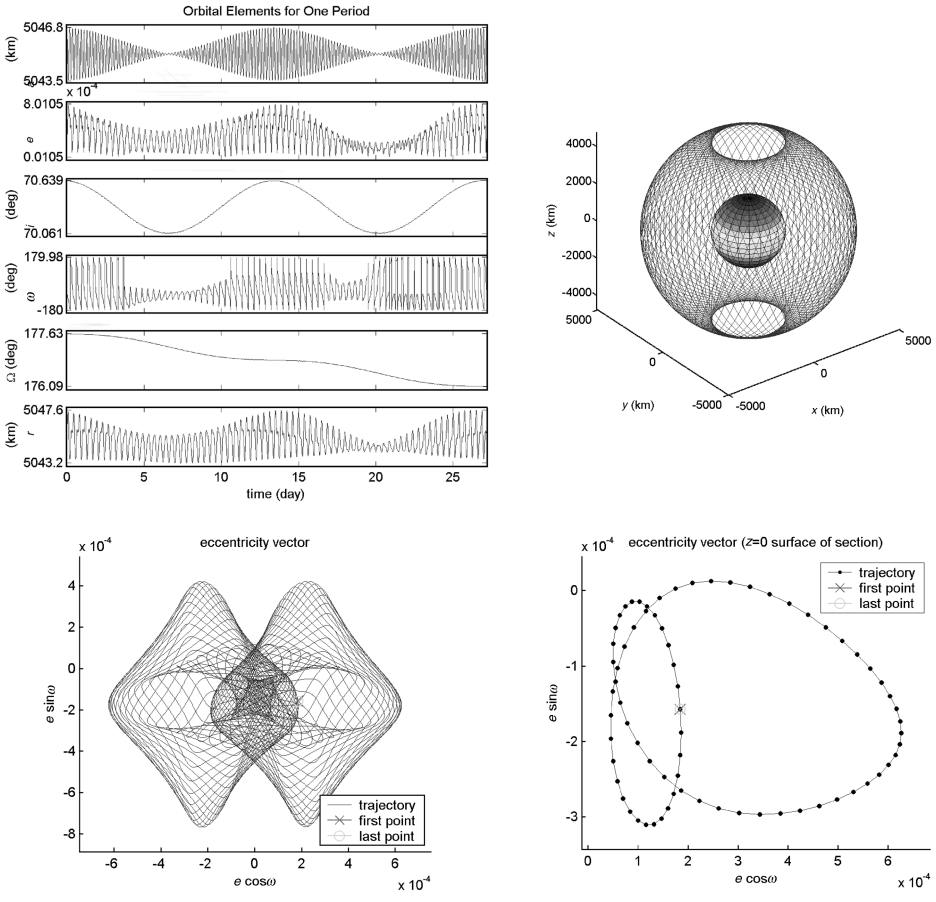

Fig. 5 Characteristics of example near-circular 73-cycle RGT periodic orbit (orbit A).

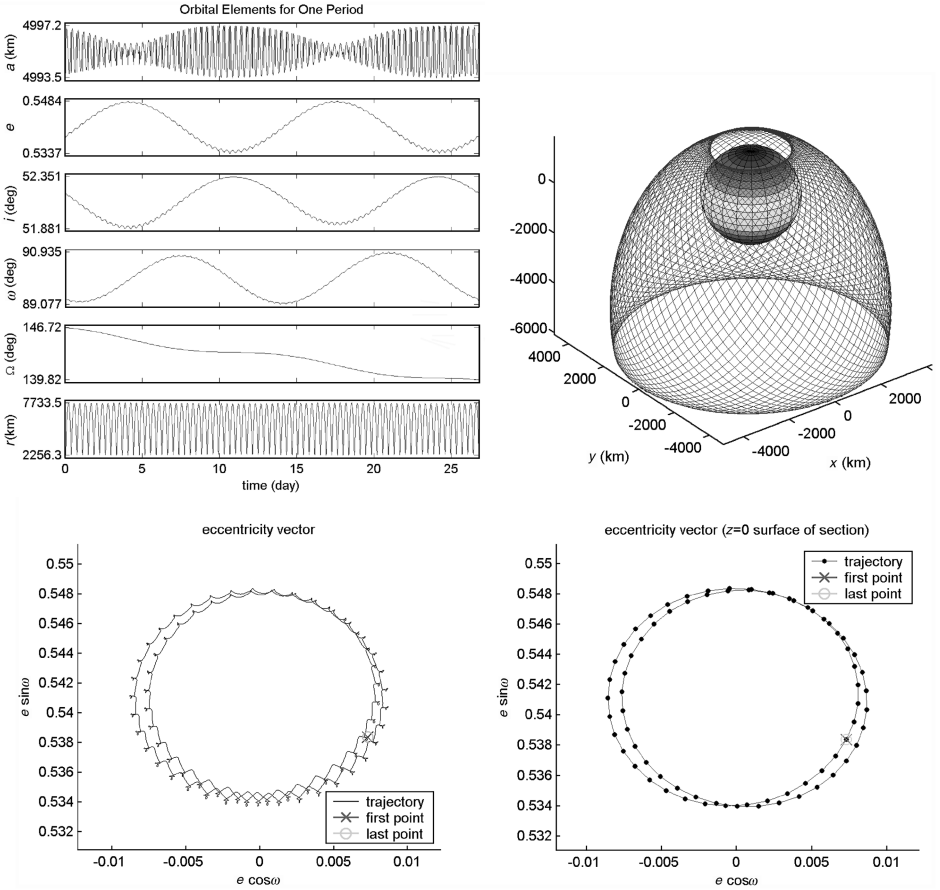

Fig. 6 Characteristics of example eccentric 73-cycle RGT periodic orbit (orbit B).

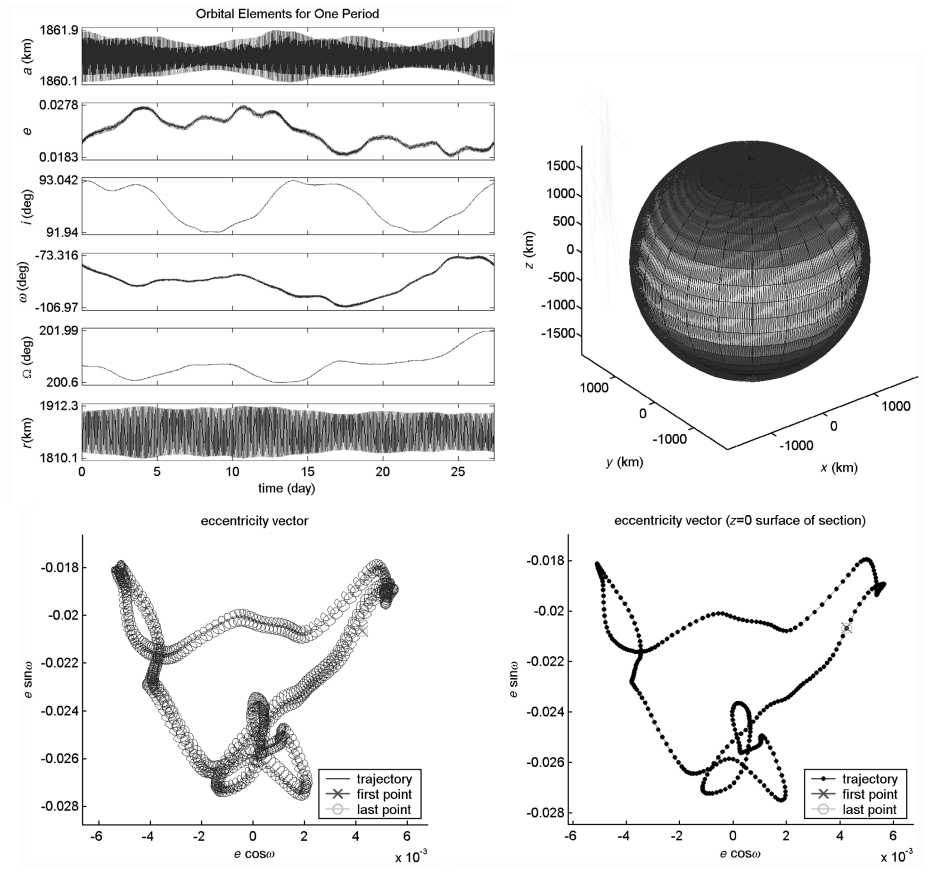

Fig. 7 Characteristics of example near-circular 328-cycle RGT periodic orbit (orbit C).

Table 2 Example orbit data ($z_0 = 0$, $v_0 = -\omega_0$)

Property	Units	Orbit A (73-cycle)	Orbit B (eccentric 73-cycle)	Orbit C (328-cycle)
x_0	LU	−1.311519120505E − 02	−7.660645625403E − 03	−4.498948742093E − 03
y_0	LU	5.435394815081E − 04	5.028162133106E − 03	−1.731769313131E − 03
u_0	LU/TU	−1.281711107594E − 02	1.327777508469E − 01	−6.203996010078E − 02
v_0	LU/TU	−3.056086111584E − 01	−9.233621714500E − 01	7.000280770869E − 02
w_0	LU/TU	9.077797920947E − 01	9.132878998189E − 01	1.588813067177E + 00
C	LU^2/TU^2	3.885779329543E + 00	3.899472252543E + 00	5.460492546479E + 00
a_0	km	5.046738218681E + 03	4.996647749602E + 03	1.861791339407E + 03
e_0	-	2.425326521133E − 04	5.384086098625E − 01	2.110475283361E − 02
i_0	deg	7.063797094157E + 01	5.220698531621E + 01	9.298309204740E + 01
ω_0	deg	−4.048674547795E + 01	8.922084663298E + 01	−7.839337618501E + 01
Ω_0	deg	1.776268201967E + 02	1.467205983429E + 02	−1.589469097527E + 02
T	day	2.716778449596E + 01	2.676187032099E + 01	2.735409767795E + 01
avg. i	deg	70.4	52.1	92. 5

presence of step function shifts in mean ω is consistent with results from [7,9], although the exact locations vary because of the different gravity fields and levels of model fidelity.

The bottom rows of Figs. 5–7 show the evolution of the tip of the eccentricity vector for the example RGT solutions. The full trajectory path is given as well as a discrete map illustrating the xy-plane crossings. These meandering paths close after one period and repeat indefinitely for a spacecraft that remains on an RGT solution. The eccentricity vector plots are useful tools for the visualization and analysis of the long-term stability of frozen and near-frozen orbits [3,5,7,8,11,12,14,15,17,39,40]. In particular, [3,11,39] rely heavily on these plots in the context of orbit maintenance for low-altitude, near-circular lunar orbiters similar to orbit C.

The orbit propagations are performed using a Runge–Kutta 7(8) integrator and the step sizes are chosen such that the Jacobi constant C is conserved to at least 13 digits over the course of a full period. The computational times per iteration of a point solution are ∼20 and ∼90 s on 3.2 GHz Xeon processor for the 73- and 328-cycle trajectory, respectively.

Long-Term Propagations

A numerically propagated orbit suffers from roundoff and truncation errors that emulate small perturbations to a spacecraft trajectory. For an unstable reference orbit, these perturbations grow with a characteristic time directly related to the magnitude of the largest eigenvalue of the Monodromy matrix (and consequently the largest stability index). A stable orbit, on the other hand, will generally be robust to the small numerical perturbations in the context of long-term stability. Figure 8 illustrates a long propagation of the mildly unstable high-altitude orbit A. Although the RGT condition is nearly maintained for the first 11 years, the eccentricity grows exponentially and finally suffers a lunar impact after 15.7 years. Twenty-year propagations of the stable eccentric orbit B and the stable low-altitude orbit C yield repeated eccentricity vector paths that are indistinguishable from those illustrated in Figs. 6 and 7.

Although the RTBP represents the motion of the moon and the Earth well to first order, the effects of considering a more realistic model represent perturbations to the system that are many orders of magnitude greater than those that result from numerical error. This is especially true at the moon where its mean eccentricity is far from zero at 0.06 and solar perturbations are significant. As an example of the solar effects, the lunar true period varies on the order of ±3 h over the course of several periods. To test the validity of the solutions in the context of these realistic perturbations, long-term propagations using the ephemeris force model (described in an earlier section) are performed. An arbitrary epoch of 12:00 1-1-2010 (Julian Date = 2,455,198.0) is used for the initial conditions.

We note again that the simplified model considers the lunar orbit and equator planes identical. In reality, there is a 5.2 deg relative inclination. To emphasize the most relevant perturbations, the initial conditions from Table 2 are applied in a reference frame based on the orbital plane for the higher-altitude orbits (A and B) and the IAU body-fixed Moon frame [24] for the lower orbit (C). For the higher altitude orbits the initial condition reference frame has its x-axis and z-axis defined at epoch as the instantaneous Earth direction and system angular momentum, respectively.

Figures 9–11 illustrate ephemeris propagations for each of the example orbits A–C, respectively. The left side of each figure shows the full path of the eccentricity vector for the first period, whereas the right side gives the xy-plane crossings for the long runs. The reported e and ω values are expressed in the ecliptic J2000 frame. Although the eccentricity vector path of the first period of orbit A is similar to the perturbed RTBP version (see bottom left of Fig. 5), the long-term instability is greater in the real ephemeris and the orbit suffers a lunar impact after 5.39 years.

As evidenced by the nonclosed eccentricity vector path after the first period, the left side of Fig. 10 shows the inability of orbit B to maintain the RGT orbit in the ephemeris model. The radius of the stability region associated with this stable eccentric orbit in the perturbed RTBP appears too small to overcome the ephemeris perturbations. Despite falling off of the RGT path, the orbit does find long-term stability as seen in the long-period libration in the $e\omega$ plane

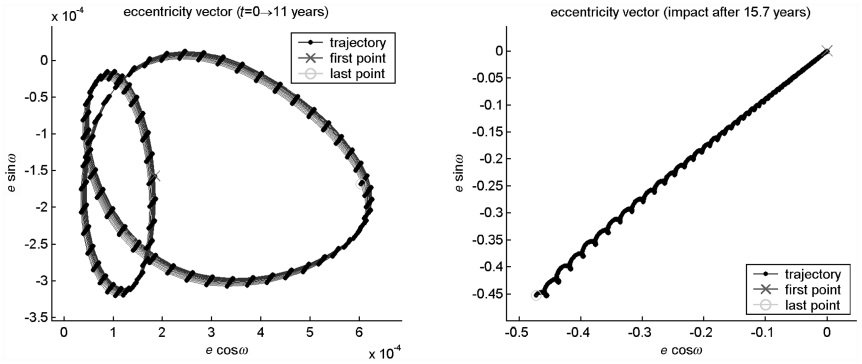

Fig. 8 Eccentricity vector at the xy-plane crossings of a long propagation (RTBP plus 50 × 50 lunar gravitational model) of the mildly unstable 73-cycle orbit A. Left: the first 11 years. Right: the full 15.7-year propagation ending at impact. Note the difference in axis scales.

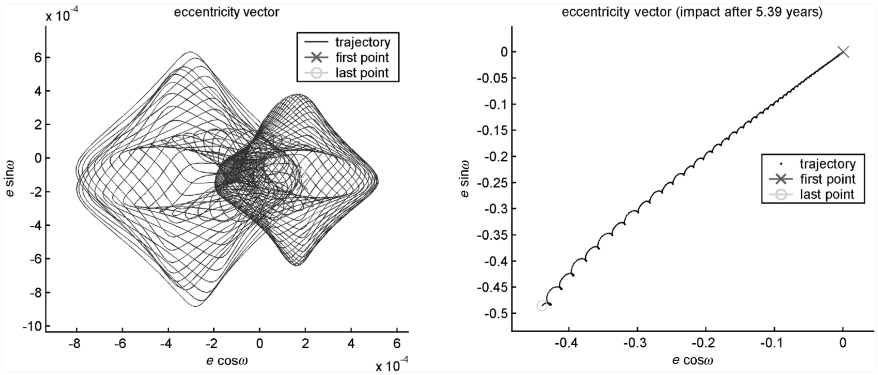

Fig. 9 Ephemeris propagation of the mildly unstable 73-cycle orbit A. Left: one period (compare to the bottom left of Fig. 5). Right: 5.56-year propagation ending with impact.

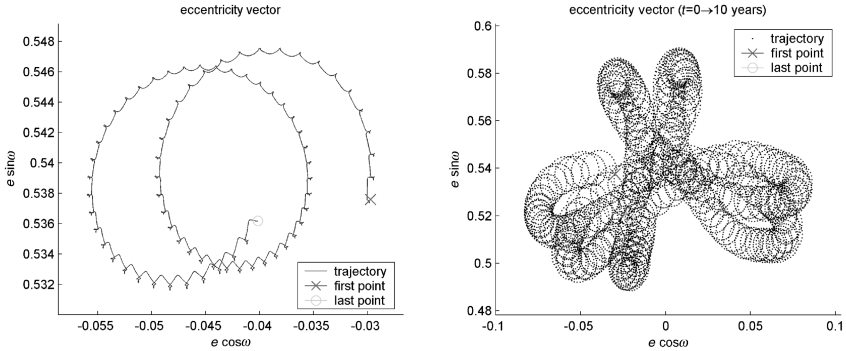

Fig. 10 Ephemeris propagation of the stable eccentric 73-cycle orbit B. Left: one period (compare to the bottom left of Fig. 6). Right: surface of section ($z = 0$) map of 10-year propagation.

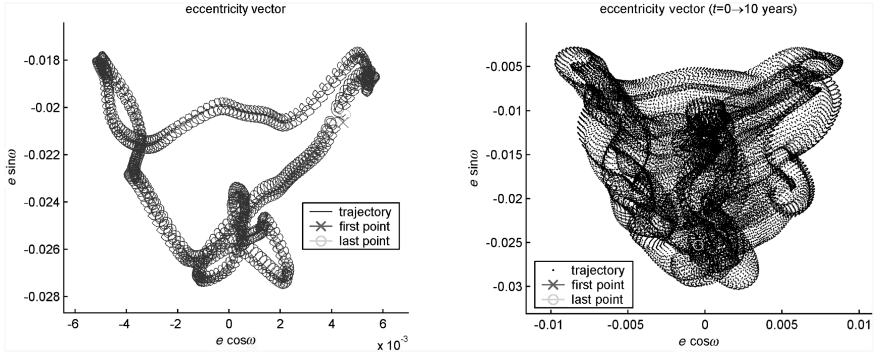

Fig. 11 Ephemeris propagation of the stable 328-cycle orbit C. Left: one period (compare to the bottom left of Fig. 7). Right: surface of section ($z = 0$) map of 10-year propagation.

with amplitudes in $\Delta e \sim 0.1$. This motion is consistent with the dynamics predicted by the simpler RTBP unperturbed by a nonspherical lunar gravity field [6,15]. Contrary to the conclusion from [16] that the effects of the sun–Earth perturbations are "rather irrelevant," Figs. 9 and 10 emphasize the importance of including accurate Earth and sun models when investigating long-term motion of high-altitude orbiters at the moon.

As expected, the agreement is qualitatively better for the case of the low-altitude near-circular orbit C, in which the assumptions of the RTBP play a much lesser role because the nonspherical gravity perturbations at this altitude are ~39 times larger (from Fig. 2) than the tidal perturbations due to the Earth. The first period of the ephemeris propagation maps an almost identical eccentricity vector path to that from the invariant model. Although the remaining ~132.4 periods do not replicate the pattern exactly, the right side of Fig. 11 shows that the orbit librates in the $e\omega$ plane with similar magnitudes. Therefore, the low-altitude, near-circular, near-polar orbit C enjoys long-term stability in an ephemeris model for at least 10 years. Similar results are found for long-term ephemeris propagations of other solutions of the 328-cycle family from Fig. 4. We emphasize that no optimizations are performed on the initial conditions.

Gravity Field Degree and Order

As mentioned, a sensitivity study in [8] on the effect of the gravity field degree on a low-altitude lunar orbiter indicates the dynamics appreciably change as the degree increases for up to at least a 50 deg field. These claims are substantiated in [23] and led to the use of the truncated 50×50 field for the bulk of the present study. However, it is natural to question the sensitivity of the current results to errors in the gravity field and the degree and order of the truncation. The error sensitivity is considered beyond the scope of the current study; however, it is acknowledged that the current lunar gravity field is limited in fidelity because of the lack of direct measurements on the far side of the moon. Regarding the truncation sensitivity, Fig. 12 presents the same 328-cycle family of the RGT orbits for a variety of different truncated versions of the lp150q gravity field. A full degree and order field and a zonal-only version are considered for degrees of 7, 20, and 50. In general, the results are consistent with the previous research that shows high sensitivity to the inclusion of the

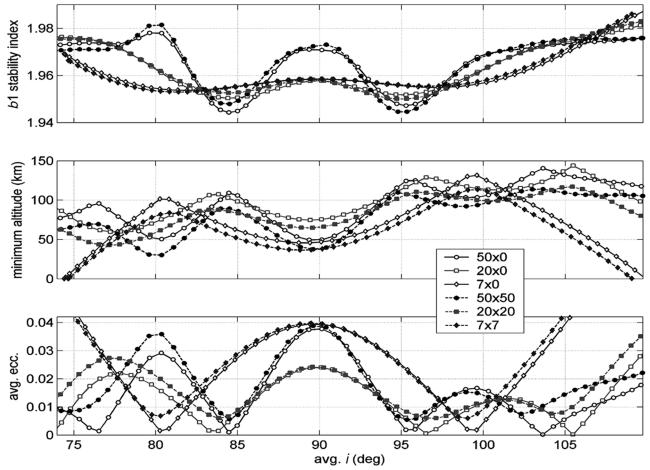

Fig. 12 The 328-cycle RGT family based on six truncated versions of lp150q gravity field.

higher-degree terms. All three of the degrees find maximums in e near $i = 90$ deg. For the inclination range considered, the degree 20 and 50 fields lead to four minimums in e, whereas the 7 deg field finds only two minimums. The locations and values of the extrema vary for each gravity field considered.

The effects of the nonzonal terms are easily seen in Fig. 12 by comparing the curves of common degree. In each case, the zonal-only curves closely approximate the full degree and order curves. The comparison does, however, reveal a positive shift in eccentricity for the nonpolar inclinations of the full degree and order families. The exactly circular solutions from the zonal-only problem are destroyed by this shift in eccentricity. The magnitude of the shift appears to increase with degree, noting that the difference in some cases is as large as $\Delta e \sim 0.01$. The lack of symmetry between the direct and retrograde periodic orbits is primarily a consequence of the third-body influence and is appreciated when the perturbation is formulated in orbital elements [41]. The nonzonal gravitational terms further destroy the symmetry about the polar orbit.

To test the practical importance of including the nonzonal terms, in Fig. 13 we compare snapshots of ephemeris propagations of two RGT solutions of the same inclination. The initial conditions for the top and bottom rows are taken from solutions based on the 50×0 and 50×50 gravity field, respectively. Both ephemeris propagations are subject to the 50×50 gravity field model and the n-body perturbations. After one period ($\sim$27 days), the two solutions trace similar $e\omega$ trajectories. However, subtle differences exist, including a significantly larger miss distance for the 50×0 solution. After 10 periods ($\sim$269 days), it is clear that the 50×0 solution departs the repeat pattern at a faster rate than the 50×50 solution. Finally, both propagations fall into a long-period libration likely related to the nutation and precession of the lunar pole. The eccentricity reaches the impact value for the 50×0 solution at 5.5 years after 74+ periods, whereas the 50×50 solution enjoys a smaller long-period Δe amplitude and remains safe for at least 10 years (134+ periods). In this example the inclusion of the nonzonal harmonic terms leads to a more favorable ephemeris trajectory.

We chose to compare the $i = 80.3$ deg solutions from Fig. 12 because of the nontrivial difference in average e. Other comparisons for solutions with different inclinations showed similar results to Fig. 13 in terms of the 50×50 solution leading to a tighter initial repeat pattern. However, in many cases the amplitude of the long-period motion in Δe is similar for the long-term propagations of both solutions, leading to 10+ year safe trajectories in either case. This is especially true when the values for average e as seen in Fig. 12 are similar for common inclinations of the 50×0 and 50×50 families. In some cases, therefore, the zonal-only solutions prove sufficient for finding long-life ephemeris orbits. We emphasize that these are preliminary tests only. A detailed ephemeris study is beyond the present scope.

The increase in fidelity of using a full degree and order field does come at a substantial cost. Including all of the computations, the run time per iteration for a solution in the 50×50 field increases by a factor of $\sim$30 compared to the zonal-only 50×0 field. Despite the

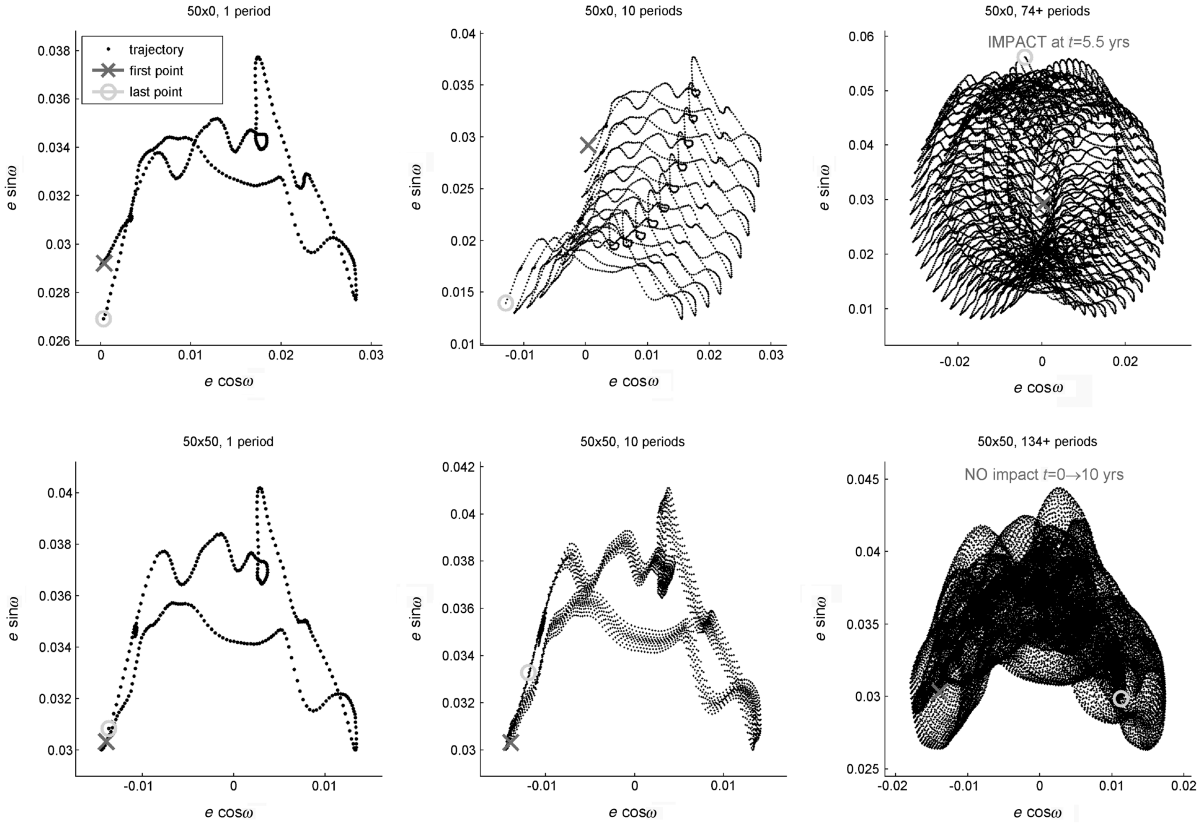

Fig. 13 Surface of section ($z = 0$) maps of eccentricity vector. Top and bottom rows are the 50 × 0 and 50 × 50 RGT solutions (with $i = 83.2$ deg from Fig. 12), respectively, propagated in the ephemeris plus 50 × 50 field.

speed penalty, the generation of the high-fidelity 328-cycle family in a 50×50 field requires one overnight job on a single 3.2 GHz Xeon processor. In contrast, the lower-fidelity families consisting of the zonal terms only (plus the third-body effects) are generated in just a few minutes, enabling rapid analysis for a variety of mission design applications.

Note that the higher-altitude orbits are intrinsically faster to generate because each period requires fewer cycles. Furthermore, they are less susceptible to the higher-order effects of the nonzonal terms. Therefore, the high-altitude orbits that remain far from the lunar surface are sufficiently modeled using the zonal terms only. It is emphasized that the computational run time is nearly a linear function of the number of cycles required to close a given RGT orbit. The slow rotation rate of the moon requires over 300 cycles for the low-altitude RGT orbits, whereas the low-altitude RGT orbits at Europa, for example, require approximately 40 cycles [17]. Thus, the run times found in the current RGT lunar application are generally an order of magnitude greater than those expected for analogous applications (RGT orbits that close after one body revolution) at most other celestial bodies of interest.

Conclusions

This study presents an alternative systematic method for finding long-life orbits around the moon. The RGT periodic orbits are demonstrated and characterized in the Earth–moon RTBP perturbed by a high-resolution lunar gravity field. The families of periodic orbits are found to be subsets of the classic frozen lunar orbits from the literature. However, the RGT orbits represent higher-order solutions because they additionally include the unaveraged equations of motion, the nonzonal harmonic terms, and the tidal forces from the RTBP. Because these solutions exist for most altitudes and inclinations, and they are not limited to small eccentricity, moon RGT orbits are useful for a variety of applications. Further, in the case of a negligible third body, the RGT periodic orbits have potential applications at Earth and Mars where high-fidelity gravity field models are known.

The described differential correction technique uses singular value decomposition to remove the degeneracies that typically plague full-dimensioned searches for periodic orbits. The correction method is systematic and shown to be efficient for finding single solutions and following families of solutions. The technique is applicable for many types of periodic orbit searches: symmetric and asymmetric, not limited to the class of high-resonant orbits studied here.

Because of the ephemeris perturbations, we find that the exactly repeating ground tracks of the lunar full potential plus RTBP are destroyed to varying degrees depending on altitude. The better agreement between the time-invariant model and ephemeris occurs for low-altitude orbits, in which the high degree and order gravity potential is identical to that included in the invariant model. As altitude increases and approximations of the RTBP deteriorate, the ephemeris solutions are less accurately predicted by the invariant model and require further tuning to optimize lifetimes. For the higher-altitude orbits, the general techniques described in this study will find better application in planetary moon systems that are more accurately modeled with the RTBP.

The low-altitude, near-circular RGT families are shown to be stable for a wide range of useful altitudes and inclinations. The solutions find strong enough resonance in the highly nonspherical lunar gravity field to overcome the ephemeris perturbations and thus enjoy long lifetimes in the realistic model. Although the computationally inexpensive solutions to the zonal-only problem lead in some cases to long-life ephemeris orbits, the inclusion of the nonzonal terms in the computation of the RGT orbits results in smaller natural variations to the ephemeris repeat ground tracks. The long-term stability and systematic methodology makes the RGT orbits immediately applicable to current and planned lunar exploration missions requiring orbiters with close surface proximity.

Appendix: Computation of Nonspherical Gravity Field

U is the potential contribution due to the nonspherical moon and is expressed via the standard spherical harmonic expansion as

$$U = -\frac{\mu}{r}\sum_{n=8}^{\infty} J_n \left(\frac{R}{r}\right)^n P_n(\sin\phi) + \frac{\mu}{r}\sum_{n=2}^{\infty}\sum_{m=1}^{n}\left(\frac{R}{r}\right)^n (C_{n,m}\cos m\lambda + S_{n,m}\sin m\lambda) P_{n,m}(\sin\phi) \tag{A1}$$

where

$$\begin{gathered} \sin\phi = z/r \qquad \sin\lambda = y/\sqrt{x^2+y^2} \\ \sin m\lambda = 2\cos\lambda\sin(m-1)\lambda - \sin(m-2)\lambda \\ \cos\lambda = x/\sqrt{x^2+y^2} \\ \cos m\lambda = 2\cos\lambda\cos(m-1)\lambda - \cos(m-2)\lambda \end{gathered} \tag{A2}$$

P_n and $P_{n,m}$ are recursively defined in Eqs. (A3–A5):

$$\begin{gathered} P_n(\sin\phi) = \frac{2n-1}{n}\sin\phi P_{n-1}(\sin\phi) - \frac{n-1}{n}P_{n-2}(\sin\phi) \\ P_0(\sin\phi) = 1, \qquad P_1(\sin\phi) = \sin\phi \end{gathered} \tag{A3}$$

$$\begin{gathered} P_{m,m}(\sin\phi) = (2m-1)\cos\phi P_{m-1,m-1}(\sin\phi) \\ P_{1,1}(\sin\phi) = \cos\phi \end{gathered} \tag{A4}$$

for $n \neq m$,

$$P_{n,m}(\sin\phi) = \frac{2n-1}{n-m}\sin\phi P_{n-1,m}(\sin\phi) - \frac{n+m-1}{n-m}P_{n-2,m}(\sin\phi) \tag{A5}$$

Equation (A6) gives the conversion between the normalized and unnormalized coefficients:

$$\begin{gathered} J_n = \Upsilon_n \bar{J}_n \qquad C_{n,m} = \Pi_{n,m}\bar{C}_{n,m} \qquad S_{n,m} = \Pi_{n,m}\bar{S}_{n,m} \\ \Upsilon_n = \sqrt{(2n+1)} \qquad \Pi_{n,m} = \sqrt{2(2n+1)(n-m)!/(n+m)!} \end{gathered} \tag{A6}$$

For the practical computations, the gradient of U is simpler if performed in the spherical coordinates and rotated back to the body-fixed frame as shown in Eq. (A7). The gradient equations are left out for brevity. The presented equations are summarized from [25]. For more details on the spherical harmonic expressions, see [25,42]:

$$\begin{bmatrix} \partial U/\partial x \\ \partial U/\partial y \\ \partial U/\partial z \end{bmatrix} = \begin{bmatrix} \cos\phi\cos\lambda & -\sin\lambda & -\sin\phi\cos\lambda \\ \cos\phi\sin\lambda & \cos\lambda & -\sin\phi\sin\lambda \\ \sin\phi & 0 & \cos\phi \end{bmatrix} \begin{bmatrix} \partial U/\partial r \\ (1/r\cos\phi)\partial U/\partial\lambda \\ (1/r)\partial U/\partial\phi \end{bmatrix} \tag{A7}$$

Acknowledgments

R. R. thanks Al Cangahuala for travel support. M. L. thanks support from projects ESP2004-04376 and ESP2005-07107 of the Spanish Government. Part of this work was carried out at the Jet Propulsion Laboratory, California Institute of Technology, under a contract with the National Aeronautics and Space Administration.

The authors thank Alex Konopliv for contributing discussions and references.

References

[1] "The Vision for Space Exploration," NASA, Publ. NP-2004-01-334-HQ, Feb. 2004.

[2] "2006 NASA Strategic Plan," NASA, Publ. NP-2006-02-423-HQ, 2006.

[3] Cook, R. A., and Sweetser, T. H., "Orbit Maintenance for Low-Altitude Near-Circular Lunar Orbits," AAS Paper 92-185, Feb. 1992.

[4] Meyer, K. W., Buglia, J. J., and Desai, P. N., "Lifetimes of Lunar Satellite Orbits," NASA Technical Paper 3394, March 1994.

[5] Ely, T., "Stable Constellations of Frozen Elliptical Inclined Lunar Orbits," *Journal of the Astronautical Sciences*, Vol. 53, No. 3, 2005, pp. 301–316.

[6] Ely, T., "Constellations of Elliptical Inclined Lunar Orbits Providing Polar and Global Coverage," AAS Paper 05-343, Aug. 2005.

[7] Cook, R., "The Long-Term Behavior of Near-Circular Orbits in a Zonal Gravity Field," AAS Paper 91-463, Aug. 1991.

[8] Konopliv, A. S., Sjogren, W. L., Wimberly, R. N., Cook, R. A., and Vijayaraghavan, A., "A High Resolution Lunar Gravity Field and Predicted Orbit Behavior," AAS Paper 93-622, Aug. 1993.

[9] Park, S. Y., and Junkins, J. L., "Orbital Mission Analysis for a Lunar Mapping Satellite," *Journal of the Astronautical Sciences*, Vol. 43, No. 2, 1995, pp. 207–217.

[10] Elipe, A., and Lara, M., "Frozen Orbits About the Moon," *Journal of Guidance, Control, and Dynamics*, Vol. 26, No. 2, 2003, pp. 238–243.

[11] Folta, D., and Quinn, D., "Lunar Frozen Orbits," AIAA Paper 2006-6749, Aug. 2006.

[12] Coffey, S., Deprit, A., and Deprit, E., "Frozen Orbits for Satellites Close to an Earth-Like Planet," *Celestial Mechanics and Dynamical Astronomy*, Vol. 59, No. 1, 1994, pp. 37–72.

[13] Rosborough, G. W., and Ocampo, C. A., "Influence of Higher Degree Zonals on the Frozen Orbit Geometry," AAS Paper 91-428, Aug. 1991.

[14] Paskowitz, M. E., and Scheeres, D. J., "Transient Behavior of Planetary Satellite Orbiters," AAS Paper 05-358, Aug. 2005.

[15] Broucke, R. A., "Long-Term Third-Body Effects via Double Averaging," *Journal of Guidance, Control, and Dynamics*, Vol. 26, No. 1, 2003, pp. 27–32.

[16] D'Avanzo, P., Teofilatto, P., and Ulivieri, C., "Long-Term Effects on Lunar Orbiter," *Acta Astronautica*, Vol. 40, No. 1, 1997, pp. 13–20.

[17] Lara, M., and Russell, R. P., "Computation of a Science Orbit About Europa," *Journal of Guidance, Control, and Dynamics*, Vol. 30, No. 1, 2007, pp. 259–263.

[18] Lara, M., Russell, R. P., and Villac, B., "On Parking Solutions Around Europa," AAS Paper 05-384, Aug. 2005.

[19] Gomez, G., Lara, M., and Russell, R., "A Dynamical Systems Approach to the Design of the Science Orbit around Europa," ISTS Paper 2006-d-02, 2006.

[20] Lara, M., "Searching for Repeating Ground Track Orbits: A Systematic Approach," *Journal of the Astronautical Sciences*, Vol. 47, Nos. 3–4, 1999, pp. 177–188.

[21] Lara, M., "Repeat Ground Track Orbits of the Earth Tesseral Problem as Bifurcations of the Equatorial Family of Periodic Orbits," *Celestial Mechanics and Dynamical Astronomy*, Vol. 86, No. 2, 2003, pp. 143–162.

[22] Wiesel, W. E., "Relative Satellite Motion About an Oblate Planet," *Journal of Guidance, Control, and Dynamics*, Vol. 25, No. 4, 2002, pp. 776–785.

[23] Roncoli, R. B., "Lunar Constants and Models Document," JPL D-32296, Jet Propulsion Laboratory, Pasadena, CA, Sept. 2005, Sec. 2.1.

[24] Seidelmann, P. K., Abalakin, V. K., Bursa, M., Davies, M. E., de Bergh, C., Lieske, J. H., Oberst, J., Simon, J. L., Standish, E. M., Stooke, P., and Thomas, P. C., "Report of the IAU/IAG Working Group on Cartographic Coordinates and Rotational Elements of the Planets and Satellites: 2000," *Celestial Mechanics and Dynamical Astronomy*, Vol. 82, No. 1, 2002, pp. 83–111.

[25] Tapley, B. D., Schutz, B. E., and Born, G. H., *Statistical Orbit Determination*, Elsevier Academic Press, Burlington, MA, 2004, Sec. 2.3.

[26] Howell, K., "Three-Dimensional, Periodic, 'Halo' Orbits," *Celestial Mechanics*, Vol. 32, No. 1, 1984, pp. 53–71.

[27] Ocampo, C. A., "Trajectory Optimization for Distant Earth Satellites and Satellite Constellations," Ph.D. Thesis, Dept. of Aerospace Engineering, Univ. of Colorado, Boulder, CO, Oct. 1996. pp. 18, 53.

[28] Russell, R. P., "Global Search for Planar and Three-Dimensional Periodic Orbits Near Europa," *Journal of the Astronautical Sciences*, Vol. 54, No. 2, 2006, pp. 199–226.

[29] Bellerose, J., and Scheeres, D. J., "Periodic Orbits in the Full Two-Body Problem," AAS Paper 06-169, Jan. 2006.

[30] Szebehely, V., *Theory of Orbits. The Restricted Problem of Three Bodies*, Academic Press, New York, 1967, Secs. 8.4, 8.8, 9.10.

[31] Siegel, C. L., and Moser, J. K., *Lectures on Celestial Mechanics*, Springer–Verlag, New York, 1971, pp. 139–151.

[32] Lara, M., and Pelaez, J., "On the Numerical Continuation of Periodic Orbits: An Intrinsic, 3-Dimensional, Differential, Predictor-Corrector Algorithm," *Astronomy and Astrophysics*, Vol. 389, Feb. 2002, pp. 692–701.

[33] Lay, D. C., *Linear Algebra and its Applications*, 2nd ed., Addison-Wesley, Reading, MA, 2000, pp. 466–475.

[34] Gomez, G., Llibre, J., Martinez, R., and Simo, C., *Dynamics and Mission Design Near Libration Points. Vol. 1 Fundamentals: The Case of Collinear Libration Points*, World Scientific Monograph Series in Mathematics, Vol. 2, World Scientific, Singapore, 2001, p. 94.

[35] Broucke, R., "Stability of Periodic Orbits in the Elliptic, Restricted Three-Body Problem," *AIAA Journal*, Vol. 7, No. 6, 1969, pp. 1003–1009.

[36] Battin, R. H., *An Introduction to the Mathematics and Methods of Astrodynamics*, AIAA, New York, 1987, p. 453.

[37] Nayfeh, A. H., and Balachandran, B., *Applied Nonlinear Dynamics*, John Wiley and Sons, New York, 1995, Sec. 3.2.

[38] Jupp, A. H., "The Critical Inclination: 30 Years of Progress," *Celestial Mechanics*, Vol. 43, Nos. 1–4, 1988, pp. 127–138.

[39] Folta, D., Galal, K., and Lozier, D., "Lunar Prospector Frozen Orbit Mission Design," AIAA Paper 1998-4288, Aug. 1998.

[40] Scheeres, D. J., Guman, M. D., and Villac, B. F., "Stability Analysis of Planetary Satellite Orbiters: Application to the Europa Orbiter," *Journal of Guidance, Control, and Dynamics*, Vol. 24, No. 4, 2001, pp. 778–787.

[41] San-Juan, J. F., Lara, M., and Ferrer, S., "Phase Space Structure Around Oblate Planetary Satellites," *Journal of Guidance, Control, and Dynamics*, Vol. 29, No. 1, 2006, pp. 113–120.

[42] Lambeck, K., *Geophysical Geodesy*, Clarendon Press, Oxford, 1988, Sec. 2.2.